Final draft for review

Washington State of Transportation

Final Report

AN INVESTIGATION OF UNDERWATER SOUND PROPAGATION FROM PILE DRIVING

Per G. Reinhall[1] and Peter H. Dahl[12]

[1]Department of Mechanical Engineering

[2]Applied Physics Laboratory

University of Washington

Seattle, Washington 98105-6698

reinhall@u.washington.edu

dahl@apl.washington.edu

July 2011

Table of Content

LIST OF FIGURES

Abstract

The underwater noise from impact pile driving is studied using a finite element model for the sound generation and parabolic equation model for propagation. Results are compared with measurements using a vertical line array deployed during at the Vashon Island ferry terminal near Seattle in November 2009. It is shown that the dominant underwater noise from impact driving is from the Mach wave associated with the radial expansion of the pile that propagates down the pile after impact at supersonic speed. The effectiveness of surrounding the pile in the water with a double walled steel tube, also called a temporary noise attenuation pile (TNAP), to reduce the underwater sound level from pile driving operations is also investigated. It is shown that the noise attenuation capability of the TNAP is limit to approximately 10 dB due to the unconstrained propagation of Mach waves directly from the sediment into the water.

1. INTRODUCTION

Pile driving in water produces extremely high sound levels in both the surrounding air and underwater environments. In terms of the underwater environment, field observations show peak acoustic pressures of $\sim 10^3$ Pa measured[1] at range 3000 m , $\sim 10^4$ Pa measured[2] at range 60 m, and $\sim 10^5$ Pa measured (this work) at range 10 m from the pile driving operation. Such pressures are known to produce deleterious effects on both fish and marine mammals[3]. As a result, pile driving has become a highly regulated construction process with significant environmental monitoring costs. Still, beyond measurements of peak and other integral measures of pressure, and related energy spectra, relatively little is known about the process of underwater sound generation and propagation from pile driving such as acoustic field variation with water depth and distribution in vertical angle. In this report we present results of a simulation and measurement of underwater noise generated from impact driving of bare (untreaded) piles and piles surrounded by a double walled steel tube, also called a temporary noise attenuation pile (TNAP). The simulation entails a full structural acoustic simulation using finite element (FE) techniques, and a parabolic wave equation (PE) simulation within a shallow water waveguide with a vertical distribution of phased point sources, as suggested by the FE results. The measurements, involving a vertical line array of hydrophones, are from a full scale pile driving test carried out at the Vashon Island ferry terminal near Seattle in November 2009.

2. UNTREATED PILES

Looking ahead, we show that the primary source of underwater sound originates from compression of the pile during pile driving. The hammer strike produces a compression wave in the pile and an associated radial displacement motion due to the effect of Poisson's ratio of steel. When the pile is surrounded by water, the speed of the downward traveling radial displacement wave (~5015 m/s) in the pile is higher than the speed of sound in the water. This produces an acoustic field in the shape of an axisymmetric cone, or Mach cone. Essential properties of the Mach cone are subsequently verified by the measurements from the vertical line array. There are, of course, additional contributions to the underwater noise field associated with pile vibrations. But it is the field associated with this Mach cone that clearly dominates peak pressure. In the following section we present results from finite element modeling of impact pile driving. In Sec. III field measurements made from a full-scale pile driving experiment are presented that relate directly to predictions made by FE analysis. In Sec. IV we present results of a companion modeling effort based on the parabolic wave equation (PE) approach with additional comparison made with the field data. Some remarks on our modeling assumptions are given in Sec. V, and a summary is given in Sec. VI.

2.1. Finite Element Analysis

To investigate the acoustic radiation due to a pile strike we created a dynamic axisymmetric finite element model of a pile being driven into the sediments in shallow water using an implicit finite element code (Comsol Multiphysics). The model was made to be consistent with one of the four piles of the 2009 Vashon Island ferry terminal test

that was a hollow steel pile, approximately 32 m (105m) long with diameter 76.2 cm (30 inch) and wall thickness 2.54 cm (1 inch). The pile was driven approximately 14 m into the sediment in water of depth 12.5 m. Cylindrical domains of water and sediment with radius of 10 m radius were included in the finite element model (See Fig.1). Perfectly matched boundary conditions were used to prevent reflections from the artificial boundaries that truncate these domains. The pile was fluid loaded via interaction between the water and the sediment and discretized using approximately 20,100 quadratic quadrilateral Lagrange elements with an element size of 6.3 mm. The water and sediment was discretized using approximately 151,000 quadratic triangular elements. The wave propagation in the pile and the surrounding medium was modeled for 20 ms using a typical time step of 0.02 μs.

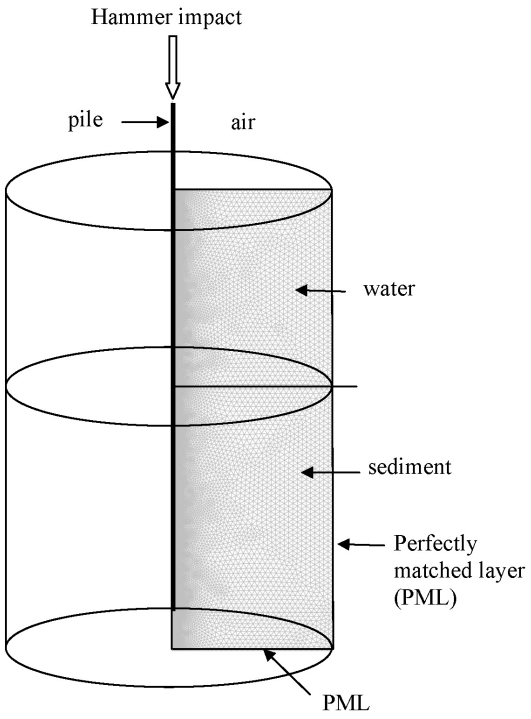

Figure 1. Axisymmetric finite element model of pile and water.

The Vashon piles were driven using a Delmag D62-22 Diesel Hammer with an impact weight of 6,200 kg and energy of 180 kNm. No cushion between the weight and pile was used. The approximate pressure, *p(t)*, resulting from the impact between the hammer weight and the pile was determined by an axisymmetric finite element impact analysis. For this purpose, the effect of the water and sediment was assumed to be negligible and only the hammer weight and the pile were model using quadrilateral Lagrange elements without taking the fluid structure into account. The impact weight was set to have an initial downward velocity of 7.6 m/s. It was found that the average pressure across the top of the pile during impact could be approximated by $p(t) = 2.1\ 10^8\ exp(-t/\tau)$ Pa where t is time after impact in seconds and the time constant τ is equal to 0.004s. Note that rise time in stress at the interface after impact is several orders of magnitude smaller than the time constant τ so the pressure is assumed here to experience a step change at the moment of impact followed by exponential decay. This is consistent with previously published data from strain gage measurements[4]. The water sound speed, c_w, was set to 1485 m/s and the sediment was modeled as a fluid with sound speed, c_s, equal to 1625 m/s. Additional remarks on sediment modeling are given in Sec. IV.

The compression wave in the pile due to the hammer strike at the top of the pile produces a local radial deformation due to a Poisson's ratio effect (Poisson's ratio for steel is approximately 0.3). This radial deformation propagates downwards along the pile with the longitudinal wave with a speed of c_p = 5,015 m/s along the section of the pile that is surrounded by water. The axial stress wave in the pile produced by the hammer impact produces a spike in the radial velocity followed by oscillation of the pile wall after the initial wave has passed through. The propagating velocity spike produces a similar spike in the acoustic pressure along the pile wall. Figure 2 shows this pressure spike at 3

and 6 ms after impact at range 1 m from the pile wall. As an aside it is noted that the negative pressure spike initially exceeds a nominal cavitation pressure threshold that varies with depth (thin dashed line); however, the pressures are also short duration which is known to increase this threshold[5].

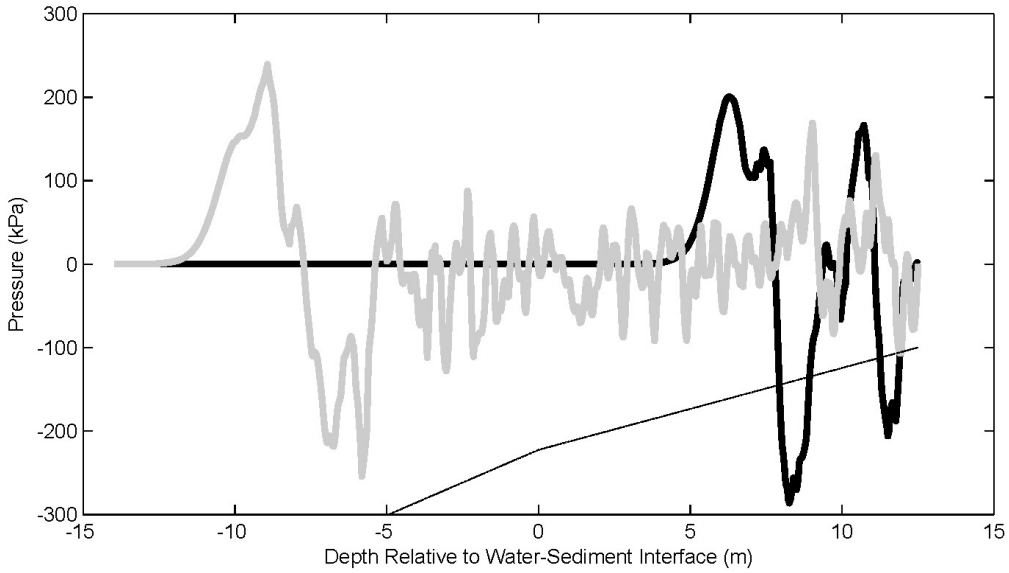

Figure 2. Acoustic pressure along the pile at a range of 1 m from the pile wall at 3 ms (black line) and 6 ms (gray line). The water surface is at z = 12.5 m. Nominal depth dependent cavitation threshold is shown by the thin line, although the actual threshold is likely to be higher owing to the short duration of the pressures.

Figure 3 shows an axisymmetric surface plot of the total acoustic pressure at 3, 6, 10 and 16 ms after impact. The supersonic (relative to the water) radial displacement wave in the pile produces an acoustic field in the water in the shape of an axisymmetric cone, or Mach cone, with its apex traveling along with the pile deformation wave front. As can be seen in Fig. 3 the initial Mach cone is followed by weaker alternating pressure variations due to oscillations of the pile wall. The radial deformation in the pile and the apex of the Mach cone reach the bottom end of the pile approximately 6 ms after impact.

It should be noted that the perfectly matched boundary conditions prevent any significant reflections from boundaries of the truncated fluid and sediment regions.

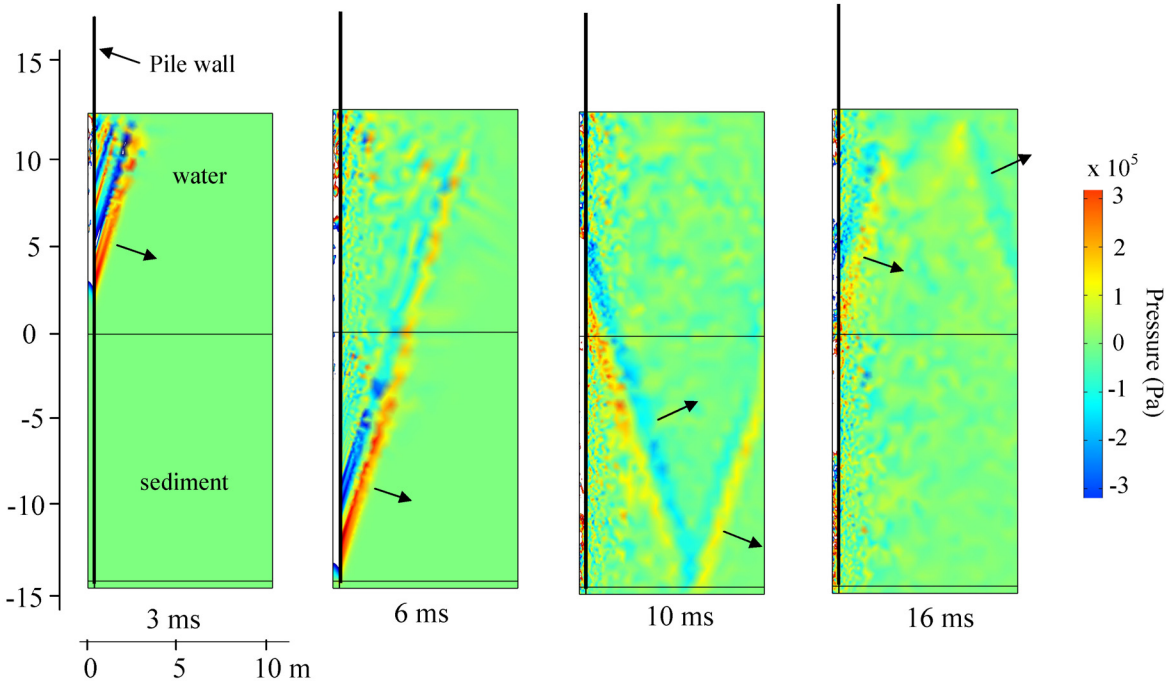

Figure 3. Acoustic pressure surface plots showing the acoustic radiation from the pile after 3, 6, 10, and 16 ms after impact by pile hammer. The propagation direction of the wave front associated with the Mach cones produced in the water and the sediment is indicated by the arrows.

A schematic of the results is shown in Fig. 4 in order to clarify the chain of events and to show propagation speeds and angles of the propagation the Mach cones. The first Mach cone is formed with a cone angle of $\varphi_w = \sin^{-1}(c_w / c_p) = 17.2^\circ$. Note that this is the angle between the vertically-oriented pile and the wave front associated with the Mach cone. This angle depends only on the two wave speeds and is independent of the distance from the pile. The Mach cone angle changes from φ_w to $\varphi_s = \sin^{-1}(c_s / c_p) = 18.6^\circ$ as the pile bulge wave enters the section of the pile that is surrounded by sediment. Note that

the pile bulge wave speed, c_p, in the sediment is slightly higher than in water due to the higher bulk modulus of the sediment and is equal to 5082 m/s.

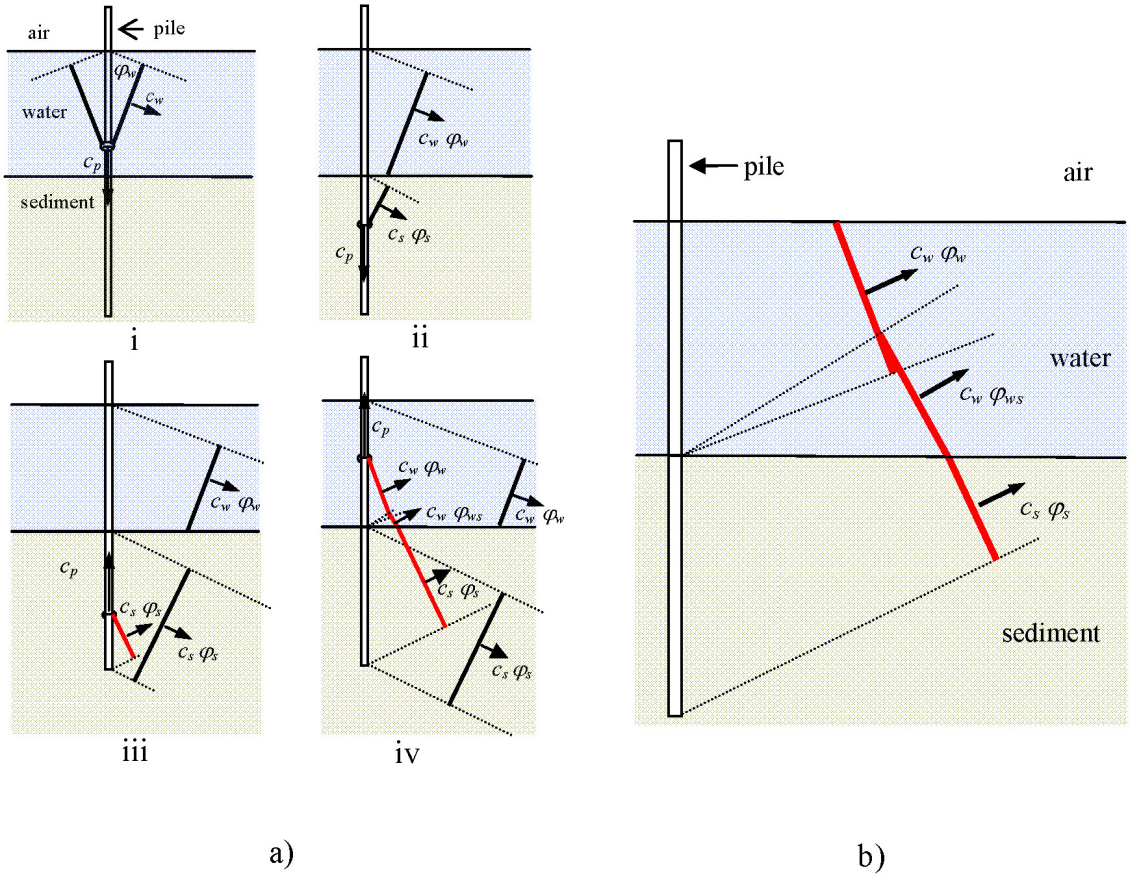

Figure 4. (a) Illustration of the propagation of the primary wave fronts associated with the Mach cone generated by the pile compression wave. i) Wave front before reaching the sediment. ii) Wave fronts after pile deformation wave have reached the sediment. iii) Wave fronts after first reflection of deformation wave. iv) Wave fronts after the reflected deformation wave have reached the water. (b) Illustration showing only the first upward traveling wave fronts after the deformation wave has reached the top of the pile.

As the deformation wave reaches the bottom end of the pile (approximately 6 ms after impact) it is reflected upwards since there is an impedance mismatch between the pile and the sediment. This reflected wave in turn produces an upward moving Mach cone of angle φ_s. The sound field associated with this cone propagates up through the

sediment and penetrates into the water, where upon φ_s changes to $\varphi_{ws} = 30.0^o$ following Snell's law. Ultimately, two upward moving wave fronts occur in the water as shown in the schematic in Fig. 4b. One with angle φ_{ws} and one with angle φ_w, the latter is produced directly by the upward moving pile wave front in the water.

It is worth noting from Figures 3 and 4 that the primary influence of the downward moving Mach cone will not be seen for depths less than D^*, where $D^* \approx R \tan\varphi_w$, and R is horizontal range from the pile source. Furthermore, the sediment-reflected wave front is significantly weaker than the incident Mach cone and cannot be observed for depth greater than D^*. There is, however, a contribution from the upward moving Mach cone within this region. These observations are important since it means that the reach of the initial and strongest acoustic wave that is associated with the downward moving Mach cone is limited to a range equal to about R^*, where $R^* \approx D / \tan\varphi_w$ and D is water depth. This will be discussed further in Section VI.

2.2 Observations (1): Time Series and Vertical Arrival Angle

An experiment to measure underwater noise from pile driving was conducted at the Washington State Ferry, Vashon Island ferry terminal in November 2009 as part of planned terminal construction project. The piles described in Sec. 2 were installed in waters of depth 12.5 m (depending somewhat on tidal range.) Underwater sound measurements were made using a vertical line array (VLA) consisting of 9 hydrophones (ITC 1042) with spacing 0.7 m, with lowest hydrophone placed 2 m above the seabed

(Fig. 5). The VLA was positioned at range 8, 12 and 15 m from the pile installation site depending on the particular test.

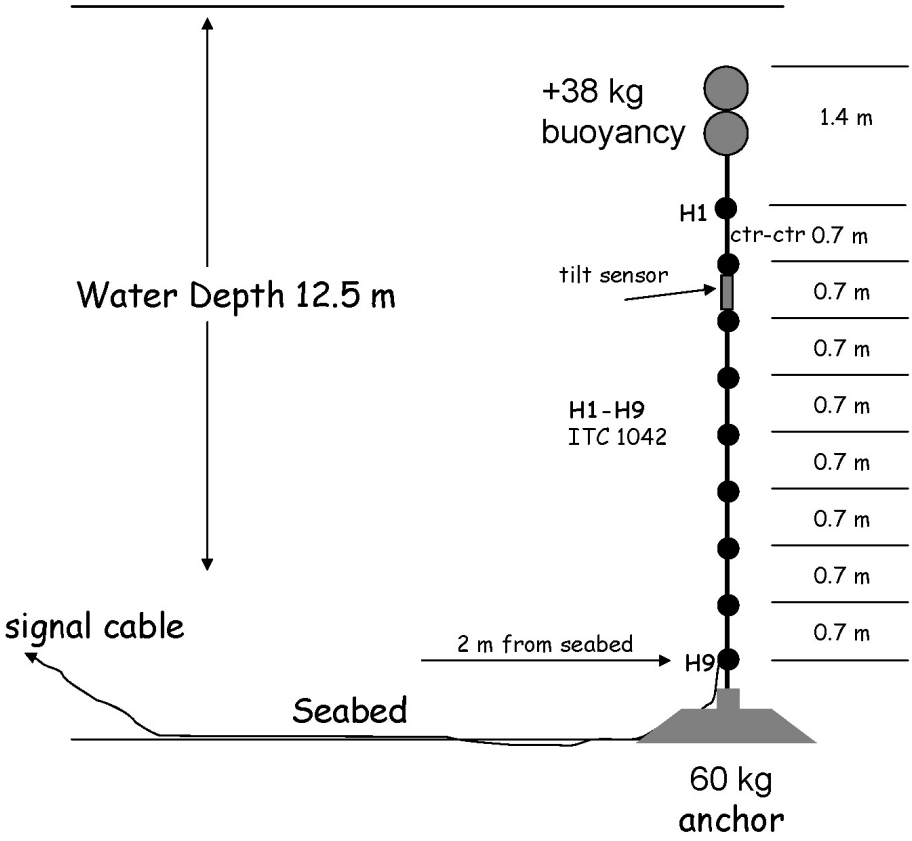

Figure.5. Vertical line array used for measurement of underwater acoustic radiation from impact installation pile driving

Acoustic data were recorded at sample rate of 62,500 Hz, with hydrophone receiving sensitivity equal to -210 dB re V/μPa (+/- 1.5 dB) without pre-amplification to avoid system network saturation from the expected high-level inputs. A pressure time series (gray lines, Fig. 6) recorded by two of the vertically separated hydrophones shows acoustic pressure originating from a pile driven by a 6,200 kg impact hammer at range 12 m from the VLA. (The data are a coherent average of 20 pile strikes that are remarkably consistent.) For reference, horizontal dotted lines show where pressure

amplitude exceeds 210 dB re 1 μPa. The effective duration of the data is 15 ms, and this can be roughly divided into three phases that we associate with the down- and up-going Mach cones. The pressure from the first and highest amplitude down-going Mach cone (phase-1is identified by the thin, black line (label 1) plotted over the data for each receiver. Shallow receivers on the VLA detect this phase first and the temporal lag, ~0.5 ms, between these two vertically separated receivers suggests a vertical arrival angle (discussed further below). Next, pressure from the first up-going Mach cone (phase-2) originating from reflection at the end of the pile, is identified by the thick, black line (label 2) also plotted over the data, and deeper receivers detect this first. We infer from both the FE analysis results in Sec. II and the field observations such shown here, that this process is repeated. Specifically, a phase-3 (label 3) is shown which is reduced in amplitude compared to phase-1, but otherwise shows the same positive-to-negative development in the pressure wave. Scaled versions of phase-1 (dashed line) are plotted over the data from each receiver at delay T sec. after the onset of phase 1 for each receiver, where T represents the nominal travel time of the bulge wave over twice the length of the pile. Here T is 12.6 ms, which puts $c_p \sim 5{,}080$ m/s or quite consistent with that predicted by the FE analysis in Sec. II.

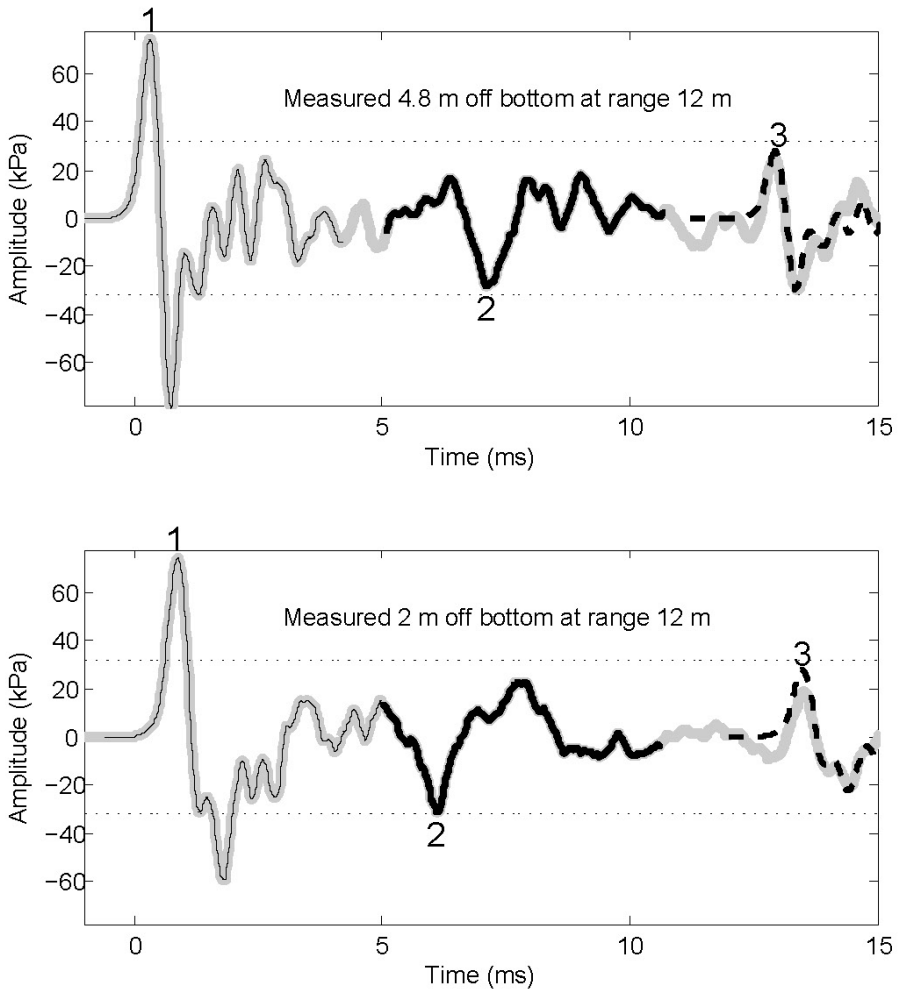

Figure 6. Pressure time series of underwater noise from impact installation pile driving measured at range 12 m at two heights above the bottom (gray lines). Horizontal dashed lines delineate a peak positive or negative pressures exceeding 210 dB re 1 μPa. The pressure from the first and highest amplitude down-going Mach cone (phase-1) is identified by the thin, black line (label 1) plotted over the data for each receiver. The pressure from the first up-going Mach cone (phase-2) is identified by the thick, black line (label 2) also plotted over the data. A phase-3 is identified for each receiver by the dashed line, in this case representing a scaled version of phase-1 (amplitude reduction 3/8) delayed by 12.6 ms.

The scaling is determined by the bulge reflection coefficient at the bottom of the pile, $\alpha \approx -3/8$, which is estimated directly from the VLA data. That is, phase-2 is approximately an inverted phase-1 with amplitude reduction of $|\alpha|$ = 3/8. As phase-3

originates from reflection from the top of the pile it undergoes a second inversion owing to the strain relief boundary condition, and thus it reverts back to the same positive-to-negative pressure development as phase-1, while maintaining an amplitude of 3/8 relative to phase-1 (i.e., no additional amplitude reduction.) Finally, we anticipate a 4th phase associated with a second reflection from the bottom of the pile, with amplitude reduction $|\alpha|^2 = 9/64$ relative to phase-1. However, this 17 dB reduction makes it more difficult to identify in the data and distinguish it from the first three and more energetic phases. Returning to the 12.6 ms T delay it is interesting to see how this is also manifested in the energy spectral density. As seen in Fig. 6 time delays between particular phases of the pulse arrival structure, e.g., between phase-1 and phase-2, will depend on depth. But common to *all* depths is the T delay. Thus, a depth-averaged energy spectral density (Fig. 7) will reveal this delay in the form of spectral interference peaks every $1/T$ Hz or 79 Hz.

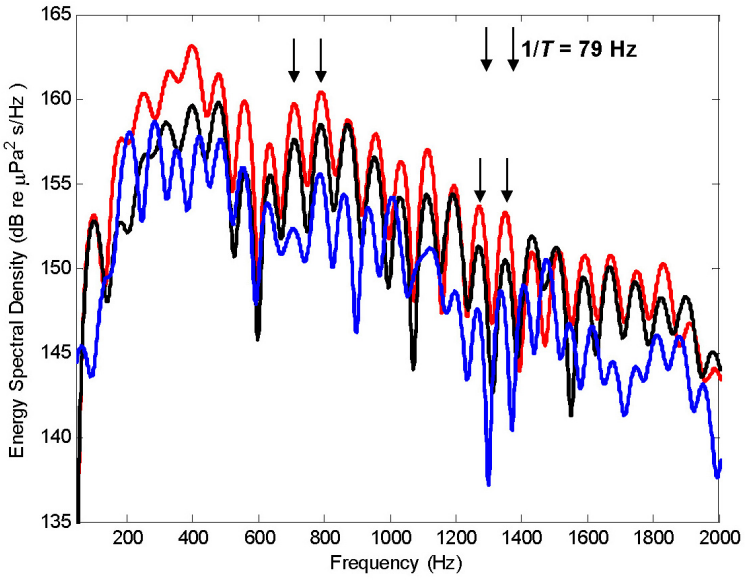

Figure 7. Energy spectral density depth averaged over the aperture of the VLA . Line color indicates particular test and VLA range from pile: 8 m (red), 12 m (black) and 15 m (blue). The spectra display prominent peaks separated by ~ 79 Hz.

The observable time lags seen in Fig. 6 between measurements made at the different heights off the bottom can be associated with a vertical arrival angle. To estimate this angle, the least restrictive approach from the stand point of source and VLA far field criteria, is one based on the time lag estimate, $\hat{\tau}$, between adjacent sensors separated by L = 0.7 m. Eight pair-wise estimates of arrival angle, $\hat{\varphi}_w = a\sin(\hat{\tau}\, c_w / L)$, are plotted as function of depth off the bottom (Fig. 8) for the three cases for which the VLA range was 8 m (red), 12 m (black) and 15 m (blue). The estimate $\hat{\tau}$ is based on cross correlation analysis of selected data segments, e.g., as indicated in Fig. 6.

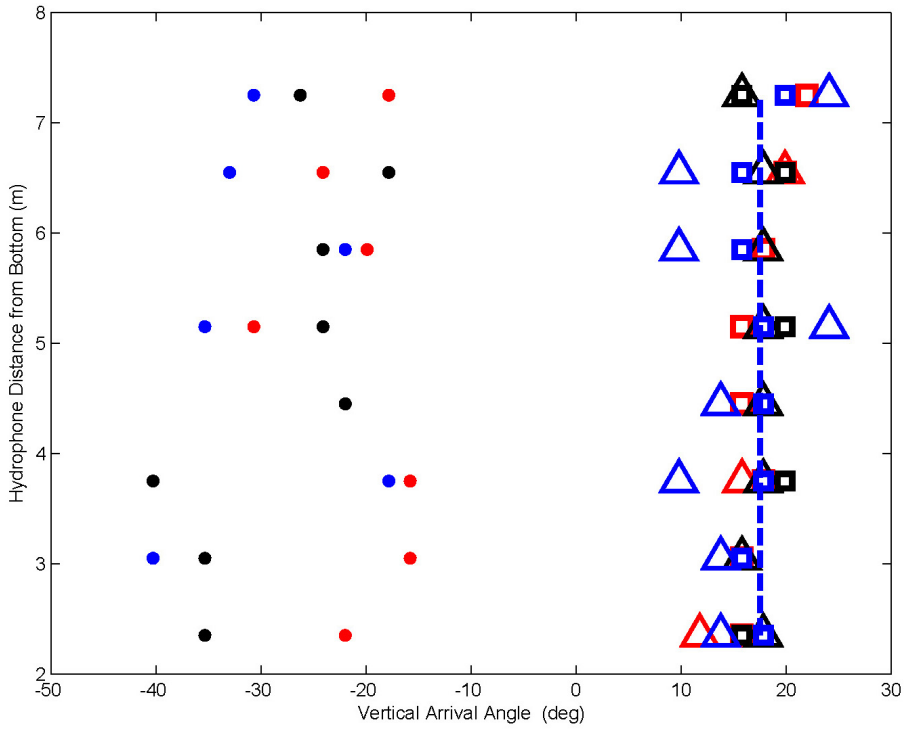

Figure 8. Estimated vertical arrival angle versus distance off the bottom for three pile driving measurement ranges. Symbol color indicates particular test and VLA range from pile: 8 m (red), 12 m (black) and 15 m (blue). The abbreviation p1, p2, and p3 in the legend indicates time periods associated with phase-1, phase-2 and phase-3 segments, respectively, are used in the estimation. The vertical line represents the mean of the phase-1 arrival angle estimates.

According to the FE results in Sec. II, there are two opportunities to measure φ_w, one being phase-1 of the pulse (i.e., label 1, Fig. 6) and the next, phase-3, approximately T ~ 13 ms later representing the field generated by the reflected bulge on the pile that has traveled twice the pile length (label 3, Fig. 6). Estimates of φ_w cluster near 17.6^o (Fig. 8, right side) a value equal to the mean of the all estimates derived from the first arrival or phase-1 segment (p1 markers), which is close to the predicted value of 17.2^o. The estimate standard deviation is ~2^o, which is somewhat greater than the Cramer-Rao lower bound as determined by signal bandwidth, signal-to-noise ration (SNR) and mean arrival angle. Interestingly, the second set of estimates of φ_w (p3 markers) also cluster about the mean but with higher variance owing to reduced SNR. An angle estimate from the first upward arrival (label 2, Fig. 6) is also possible with corresponding estimates shown on the left side of Fig. 8 (p2 markers). These represent in a sense a combined estimate of φ_w (reversed in sign) and φ_{ws} (see Fig. 4). This mixture of arrival angles along with lower SNR necessarily results in a greater spread of estimates. It is significant that the arrival angle estimates do not vary, in a mean sense, with range, over the three test ranges that span 0.75 to 1.25 water depths. This is consistent with a phased array of sources produced by the bulge on the pile traveling downward and upward at supersonic speed relative to the speed of sound in water.

2.3. Observations (2): Comparison With Parabolic Wave Equation Simulations

A broad band simulation of the received pressure pulse from impact pile driving is obtained via inverse Fourier transform of a frequency-domain solution. For this we use

the RAM (Range-dependent Acoustic Model) PE code[6] to compute the Green's function $G(\vec{r},\vec{r_i},f)$, representing the complex acoustic field at receive position vector $\vec{r}$ and frequency f that originates from a unit-strength point source at $\vec{r_i}$. It will be necessary to use multiple point sources distributed vertically over the wetted-length of the pile, as outlined further below, and sum the results to obtain the desired acoustic field in the frequency domain. This field is computed for 1024 frequencies between 50.8 Hz and 2048.8 Hz, every dF = 1.95 Hz, to accommodate a time spread of nominally 500 ms. Although the frequency-domain PE field is only supported up to ~2000 Hz, it is zero-padded up to 16000 Hz (8192*dF), prior to Fourier transforming to the time domain such that a more refined interpolation in the time domain is achieved.

The geoacoustic model is a water column of depth 12.5 m with constant sound speed equal to 1485 m/s (measured at the time of the experiment using conductivity-temperature-depth probe), and a sediment taken to be a fluid halfspace (which is ultimately terminated by an artificially high absorbing layer[7].) Boring logs from the site made prior to construction describe a mixture of sand-like sediments. Although the FE analysis results of Sec. II utilized a constant sediment speed, the longer propagation distances evaluated here may be influenced by sound speed dispersion effects. Thus we use a model for sandy sediments[8] based on Biot theory for sediment sound speed as function of frequency which puts the sound speed equal to 1600 m/s and 1680 m/s for lower and upper end of the frequency range, respectively. For sediment attenuation we use the empirical model[9] that is also consistent with Biot theory, which puts attenuation between 0.002 and 1.325 dB/m for lower and upper frequency limits. The density in the sediment is assumed to be 1.85 times that in water column.

As suggested by the both FE analysis simulation and the field observations, the Poisson's ratio coupled radial expansion, traveling down the pile at speed ~5000 m/s, and the ensuing Mach cone is responsible for the majority of the underwater sound energy observed. The PE simulations address only this feature using a vertical distribution of time-delayed, broad-band point sources, with time delay of the i^{th} source located at $\vec{r}_i$, established by its depth and the speed of the pile bulge wave, c_p = 5048 m/s. This can be also viewed as a phased array of sources for which the phase is set by the supersonic speed of the bulge. (The speed is taken to be an average of the speeds in water and sediment, although the latter is about 1% more as discussed in Sec. II.)

The PE implementation involves a distribution of 106 such point sources, at 0.25 m intervals, starting at air-water interface, spanning the water column (12.5 m) and sediment phase of the pile (14 m). To account for the pulse delay as the bulge travels down the pile, the received spectrum, from the i^{th} point source, $s_i(\vec{r}, f)$ is computed as $s_i(\vec{r}, f) = G(\vec{r}, \vec{r}_i, f) A(f) e^{i2\pi f \tau_i}$ where τ_i is the point source time delay equal to the source depth z_i divided by c_p, where z_i ranges from 0.25 m to 26.5 m, and $A(f)$ is an empirical amplitude weighting spectrum. This spectrum is constructed from an estimate of the amplitude spectrum made from data using isolated time segments associated with the first arrival, or phase-1 (e.g., as shown in Fig. 6), and further details on the estimation procedure are provided below.

The complex amplitude spectrum of the first arrival $S_1(\vec{r}, f)$, is the superposition of all the sources distributed over the wetted-length of the pile (water and sediment) as given by $S_1(\vec{r}, f) = \sum_{i=1}^{106} s_i(\vec{r}, f)$. [1]

Convergence tests were applied with different source density and spacing, for example, halving the number of sources to 53 with spacing 0.5 m, provides the same answer to within a calibration constant, as does doubling the number sources. The corresponding pressure field $p_1(\vec{r},t)$ is given by

$$p_1(\vec{r},t) = \mathrm{Re}\left[\int_o^{f\,\max} S_1(\vec{r},f)e^{-i2\pi ft}df\right] \qquad [2]$$

(carried out with inverse FFT) where $f\ max$ =16000 Hz which is linked to aforementioned zero-padding, recalling that actual support in the frequency domain is limited to about ~2000 Hz. The pressure field $p_1(\vec{r},t)$ represents a model for first arrival, or phase-1 of the data as discussed in Sec. II, Fig. 6.

The complex amplitude spectrum of the second arrival, $S_2(\vec{r},f)$ and third arrival $S_3(\vec{r},f)$, corresponding to phases 2 and 3 in Fig 6 are similarly constructed using the summation of 106 sources as in Eq. (1). Here, time delays continue to accumulate as follows: for the second arrival the time delay τ_i for each source is

$$\tau_i = (P_{wl} - z_i)/c_p + P_{wl}/c_p, \qquad [3]$$

and for the third arrival the time delay is

$$\tau_i = 2P_l/c_p + z_i/c_p \qquad [4]$$

where total pile length, P_l , is 32 m, and wetted pile length, P_{wl} is 26.5 m. For these two subsequent arrivals, the effect of amplitude and phase changes from pile-end reflections must also be included in Eq.(1); thus for $S_2(\vec{r},f)$ and $S_3(\vec{r},f)$, Eq.(1) is multiplied by -3/8 and 3/8, respectively. These complex spectra are added to $S_1(\vec{r},f)$ in Eq. (1) to obtain the total pressure field $p(\vec{r},t)$, or they can be inverse transformed separately to examine component fields. (Note that a $S_4(\vec{r},f)$ associated with phase-4

can also be similarly constructed but its overall impact on the total field is negligible as in this case the multiplier is -9/64.)

Returning to the amplitude spectrum $A(f)$, it is constructed from the data as follows: The first arrival is isolated from the three lowest hydrophone channels on the VLA (these are 2 m, 2.7 m and 3.4 m off the bottom) from which an estimate spectrum is made. These channels are selected because of their higher SNR and the first arrival, defined as the phase-1 segment of length 5 ms as shown in the lower plot of Fig 6, is more readily identified. Data from the 8-m range test are used but results are similar for the 12 and 15-m range tests. Prior to FFT analysis the segments are passed through a equal-length Tukey window (taper parameter, or ratio of taper to constant sections = 0.5) to smooth the transient effects associated with data truncation. An average of the magnitude-squared spectra from these three channels is taken from which the square-root represents our estimate of the amplitude spectrum $A(f)$ which is normalized to its maximum value. This spectrum is sub-sampled every 1.95 Hz to correspond to the PE frequencies, and it is further shaped (to a small extent) near its end points at 50.8 and 2048.8 Hz by a Tukey window (taper parameter 0.015) to reduce a ringing effect in the time domain results. The final result (Fig. 9) displays the same approximate 10 dB decrease between the peak frequency near 300 Hz and 2000 Hz as shown in Fig. 7 but without the frequency interference effects shown in the latter owing to the 12.6 ms time delay.

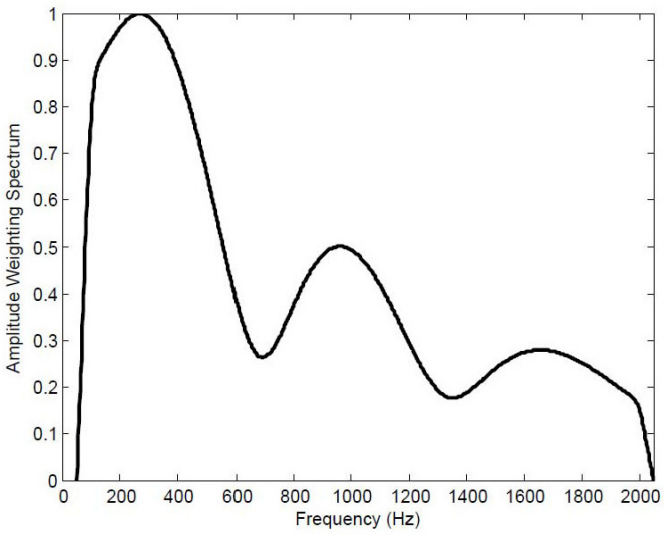

Figure 9. The amplitude weighting spectrum *A(f)* used for the PE analysis that is estimate from data (see text for estimate procedure.) Note that *A(f)* is defined every 2 Hz between 50 and 2050 Hz.

Figure 10 shows a comparison between measured first-arrival pressure amplitude as a function of hydrophone depth and range and its PE-simulated counterpart for the three ranges measured: 8 m, 12 m and 15 m. The simulated results for all ranges are given the same *single* calibration offset, 232 dB, that applies to all depths, derived from a least squares fit between the simulated data and the corresponding 27 observations representing 9 depths and 3 ranges. (From convergence testing this offset is exactly 6 dB higher if half the number of sources, i.e. 53, are used.) We note that each observation has a spread of at least +/- 1.5 dB owing to calibration uncertainty. An important observation is the apparent clustering of both the data and simulation results at all ranges to within about 2-3 dB at the lowest hydrophone depth (10.5 m or 2 m above the bottom) and corresponding spread at these ranges of about 8 dB at the shallowest depth (5 m or 7.6 m above the bottom).

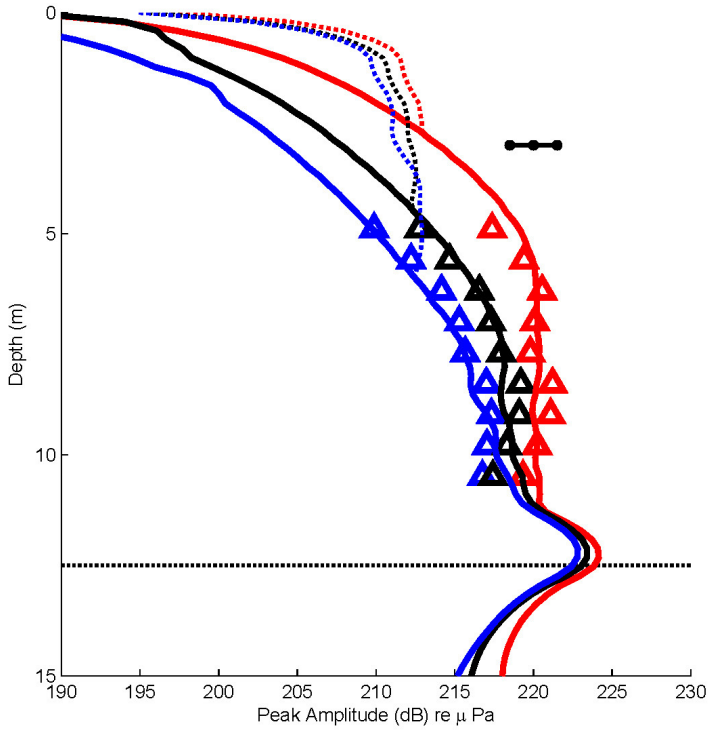

Figure 10. Measurements (symbols) of the first-arrival pressure amplitude expressed in dB re 1 μPa as a function of hydrophone depth and range representing the three measurement ranges: 8 m (red), 12 m (black) and 15 m (blue). A representative error spread is shown in upper left. The solid, thick lines with same color coding show PE-simulated counter part based on a phased-array of sources as described in the text. Note that for the measurements, the first-arrival amplitude coincides with the peak amplitude. The thin, dashed lines with same color coding show PE-simulated peak pressure amplitude which coincides with first-arrival amplitude for depths below D^*. Horizontal dotted line delineates the water sediment interface at depth 12.5 m.

For all observations at the three ranges, the pressure amplitude of the first-arrival coincides with the peak amplitude, and these observations agree well with the PE-simulated first-arrival (solid lines in Fig. 10.) It is of interest to examine the PE-simulated *peak* amplitudes (dotted lines in Fig. 10), which begin to differ from the first-arrival amplitudes at depths above D^*; this depth representing the approximate boundary of the first and primary Mach cone (see Sec. II.) However, fully capturing this

interesting feature of the pressure field with the limited number of VLA sampling depths and ranges is more difficult. Although, not explicitly verified with data from our particular field geometry, we anticipate from Fig. 10 that the maximum pressure levels will continue to be observed near the water-sediment interface out to ranges of a few depth scales. Finally, a comparison between PE-simulated and measured time series at range 12 m (Fig. 11), shows reasonable agreement over the duration of the time series (represented here as the absolute value of the Hilbert transform of both data and simulation, to which the same calibration offset, 232 dB, is applied to the latter.) To visualize time delays, a dot is placed below the peak of the first arrival in the pressure data for each channel with a second dot located on the graph exactly 12.6 ms later. The first dot nominally traces the arrival time of the down-going Mach cone and the second dot traces its repetition occurring 12.6 ms later as discussed in the context of Figs. 6 and 7. Evidence for the up-going Mach cone, more difficult to track, can be seen in the data within the 6-8 ms time window in the deepest channel and within the 8-10 ms time window in the most shallow channel.

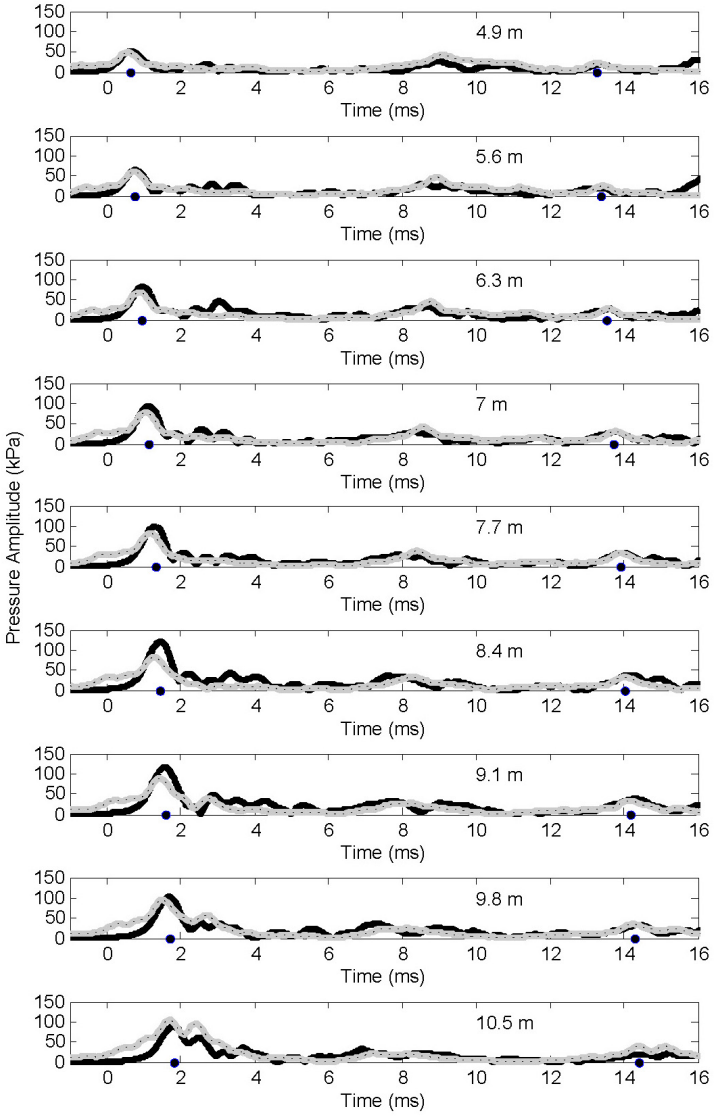

Figure 11. Comparison between measured (black lines) and PE-simulated (gray lines, dotted) time series for the 9 elements of the VLA at measurement range 12 m. Element depth is noted in each case. For the measured data, the arrival time for first and maximum arrival at each depth is identified by the black dot (left side) and a second black dot is plotted 12.6 ms after this time (right side).

3. NOISE ATTUNATION USING A TEMPORARY NOISE ATTENUATION PILE

The effectiveness of a Temporary Noise Attenuation Pile (TNAP) to reduce the underwater sound level from pile driving operations was also evaluated during the 2009 Vashon ferry terminal dolphin replacement project. To this end, a 48 feet long double

wall TNAP was constructed using two concentric pipes with outside diameters of 60 and 48 inch and a wall thickness of 1 inch (see Fig. 12). The 5 inch space between the inner and outer steel tubes was partially filled with a 4 inch thick sound absorbing material. The introduction of bubbles between the pile and the hollow tube was made possible though a bubble ring at the bottom of the TNAP.

In order to test the effectiveness of the TNAP, four 105 ft long 30 inch diameter piles were driven 35 feet into the sediment using a vibratory hammer. The TNAP was then installed (see Fig 13) around the pile and the pile was driven another 8 to 9 ft using a Delmag D62-22 Diesel Hammer with an impact weight of 6,200 kg and energy of 180 kNm as specified in Section 2.1. The last foot was driven with the TNAP removed and data was collected for the untreated pile (Section 2). This was repeated for four piles. A schematic of the TNAP concept is shown in Fig 14.

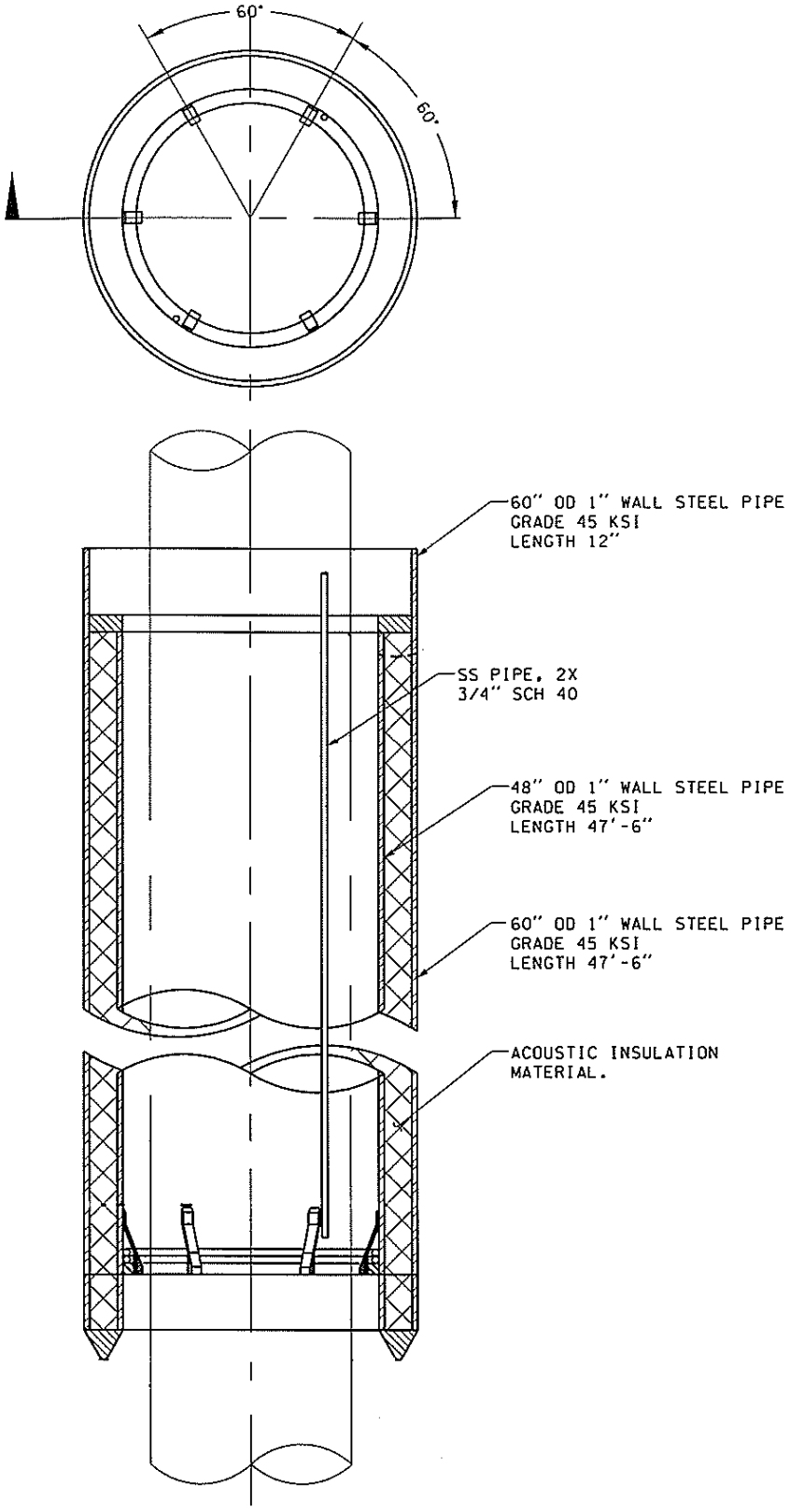

Figure 12. Sketch of the TNAP

Figure 13. Installation of the TNAP around a 30 inch diameter pile.

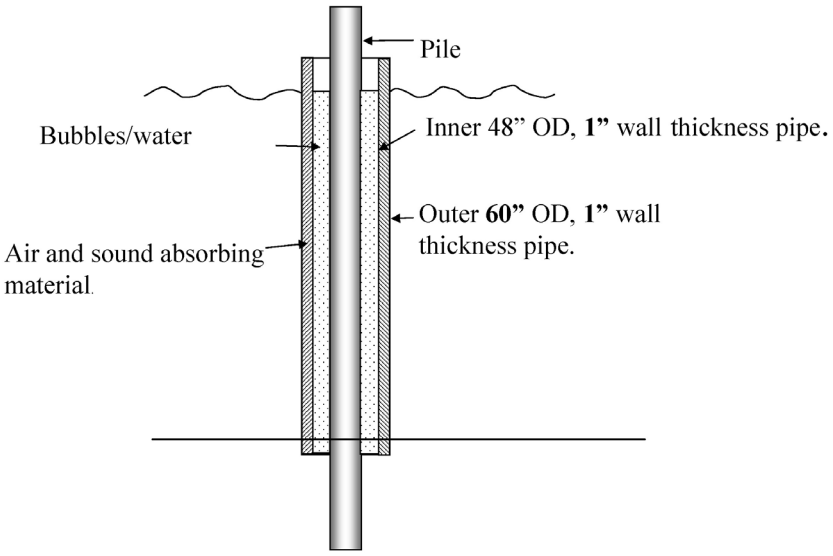

Figure 14. Schematic of the TNAP concept

3.1 Modeling Results

To investigate the acoustic radiation due to a pile strike when the pile was surrounded by a TNAP we complemented the finite element model in Section 2.1 with a detailed finite model of the TNAP. All significant components of the TNAP were modeled, including the two pipes, the sound absorbing material, the bottom steel ring and the flexible top connection.

Figure 15 shows an axisymmetric surface plot of the total acoustic pressure at 5, 8, 11, 13 and 17 ms after impact. It can be seen that the TNAP is very effective in attenuating the noise produced by the part of the pile that is submerged in the water. A significant Mach cone is not produced until the compression wave the associated radial bulge reaches the sediment leaves surrounding TNAP. The radial deformation in the pile and the apex of the Mach cone, which is now contained within the sediment only, reach the bottom end of the pile approximately 6 ms after impact. As for the untreated pile, an upward moving Mach cone is produced after the first reflection of the structural wave. At approximately 8 ms the structural wave and the apex of the upward moving Mach cone reach the TNAP and the water-sediment interface. The pile bulge is again propagating inside the TNAP and the creation of the Mach cone is essentially ceased. As can be seen in Figure 14 the upward moving Mach wave that was produced in the sediment reaches the water-sediment after 8 ms and continues to propagate up into the water.

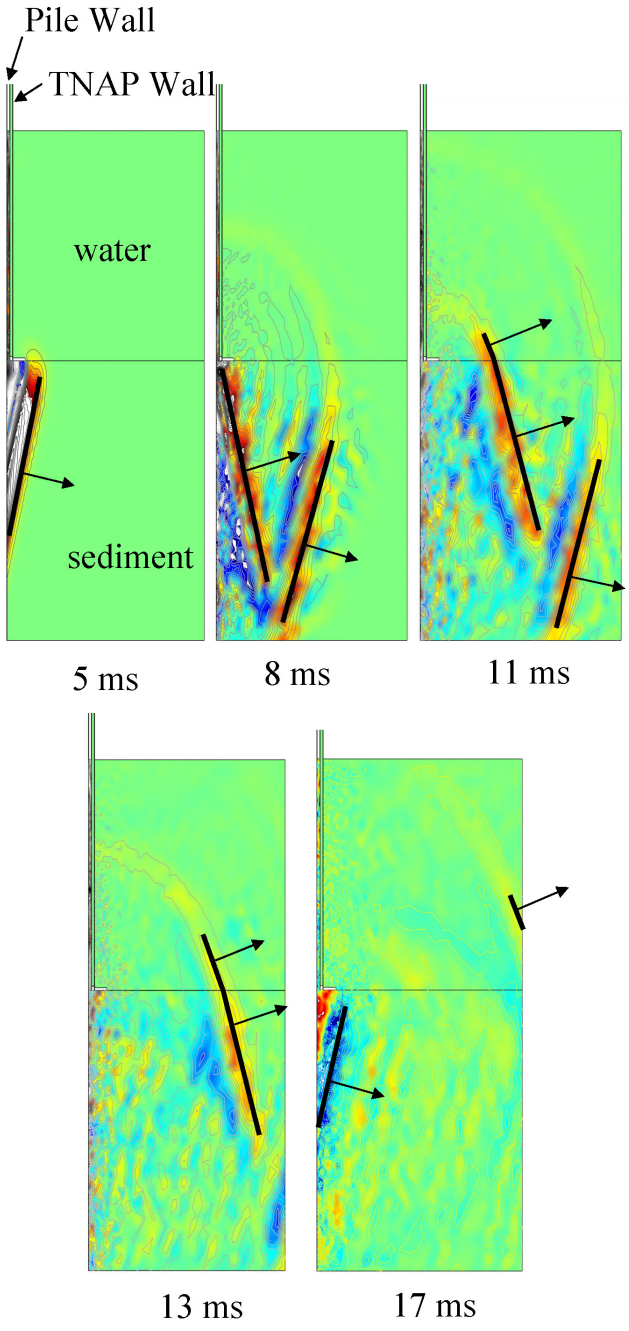

Figure 15. Acoustic pressure surface plots showing the acoustic radiation from the pile with the TNAP after 5, 8, 11, 13 and 17 ms after impact by pile hammer. The propagation direction of the wave front associated with the Mach cones produced in the water and the sediment is indicated by the arrows.

A schematic of the FE analysis results is shown in Fig. 16 in order to clarify the chain of events and compare the process to the untreated pile case. The first Mach cone is formed with a cone angle of $\varphi_s = \sin^{-1}(c_s / c_p) = 18.6^\circ$. As for the untreated case this is the angle between the vertically-oriented pile and the wave front associated with the Mach cone. As the deformation wave is reflected against the bottom end of the pile produces an upward moving Mach cone of angle φ_s. The sound field associated with this cone propagates up through the sediment and penetrates into the water, where upon φ_s changes to $\varphi_{ws} = 30.0^o$ following Snell's law. Essentially no Mach cone is produced by the upward moving pile wave front in the water. The sound field produced directly between the interface between the pile and the water is predicted by the FE to be attenuated in excess of 30 dB by the TNAP. However, the TNAP, due to its limited coverage, does nothing to decrease the Mach cone emanating from the sediment into the water

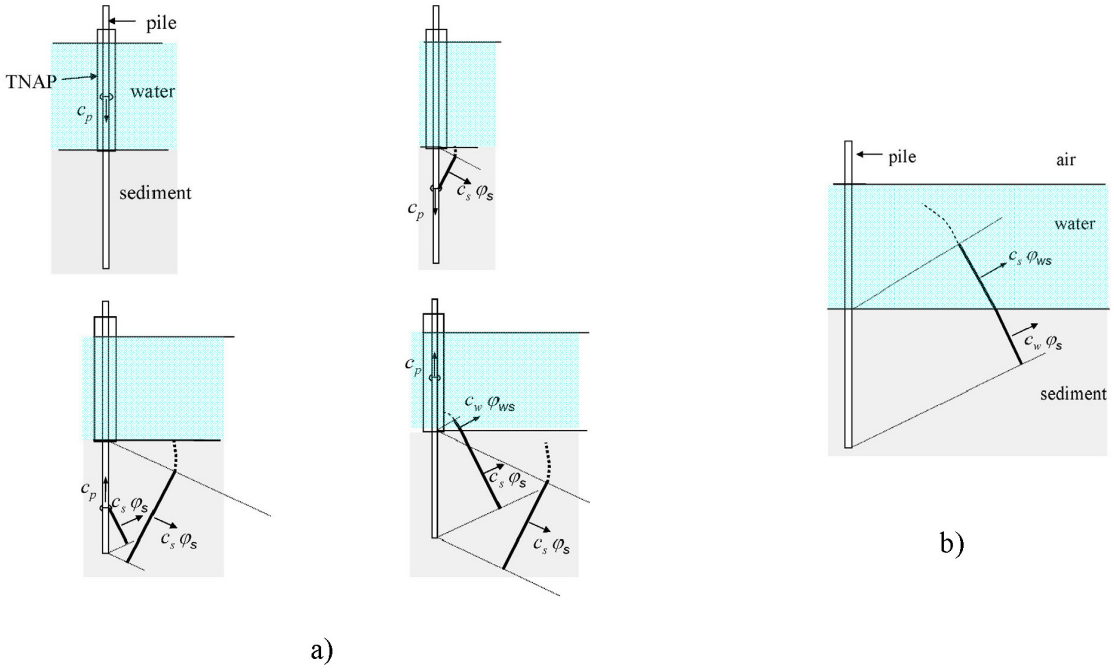

Figure 16. (a) Illustration of the propagation of the primary wave fronts associated with the Mach cone generated by the pile compression wave when the pile is surrounded by the TNAP. i) Wave front before reaching the sediment. ii) Wave fronts after pile deformation wave have reached the sediment. iii) Wave fronts after first reflection of deformation wave. iv) Wave fronts after the reflected deformation wave have reached the water. (b) Illustration showing only the first upward traveling wave fronts after the deformation wave has reached the top of the pile.

.

3.2 Field Test Results

As described in Section 2, acoustic data were recorded at sample rate of 62,500 Hz, with hydrophone receiving sensitivity equal to -210 dB re V/μPa (+/- 1.5 dB) without pre-amplification to avoid system network saturation from the expected high-level inputs. Fig. 17 shows the acoustic pressure originating from an untreated pile (black line) and a pile surrounded by a TNAP (grey line) as recorded by a hydrophone in the VLA located 4.8 m off the bottom at a range of 12 m. In both cases the pile was driven by a 6,200 kg impact hammer with an energy of 180 kNm. For reference, horizontal dotted lines show where pressure amplitude exceeds 210 dB re 1 μPa. It can be seen that the pressure

recording for the TNAP totally lacks the initial pulse of the untreated pile that is associated with the first arrival of the downward moving Mach cone (which reaches 215 dB re 1 μPa). This is the Mach cone created in the untreated case by the direct interaction between the pile and the water. The negative spike at approximately 8 ms exists for both the TNAP and the untreated case and corresponds to the arrival of the upward moving Mach cone that was created in the sediment after the first reflection of the pile bulge. This is the wave that is not hindered by the existence of the TNAP since it does not reach down into the sediment. It is seen that this spike is what limits the effectiveness of the TNAP since it results in a peak amplitude pressure during of 204 dB re 1 μPa or an 11 dB decrease compared to the maximum peak pressure for the untreated pile. (This difference actually ranges from 10 to 15 dB depending on case study, as will be shown at the end of this section.) It should also be noted that there exists a weaker spike in the TNAP pressure data at 3.5 ms, or 4.5 ms prior to the arrival of the Mach cone. This is due to a wave diffracted into the water when initial downward moving pile bulge wave leaves the TNAP. This wave takes on a circular shape in Fig. 15 and connects with the first downward moving Mach cone at the water/sediment interface.

Figure 18 show the acoustic pressure records from all nine hydrophones at a range of 12 m. The black dotted line connects the maximum amplitude peak recorded by all the hydrophones. It can be seen by the slope of this line that the Mach wave arrives at the lowest hydrophone first. The angle of the upward moving Mach wave is estimated from the measured data to be equal to 34^{o}. This is a clear experimental confirmation of the modeling results presented in the previous section. The small error in the angle of the Mach cone is most likely due to a difference between the actual and estimated wave speed in the sediment.

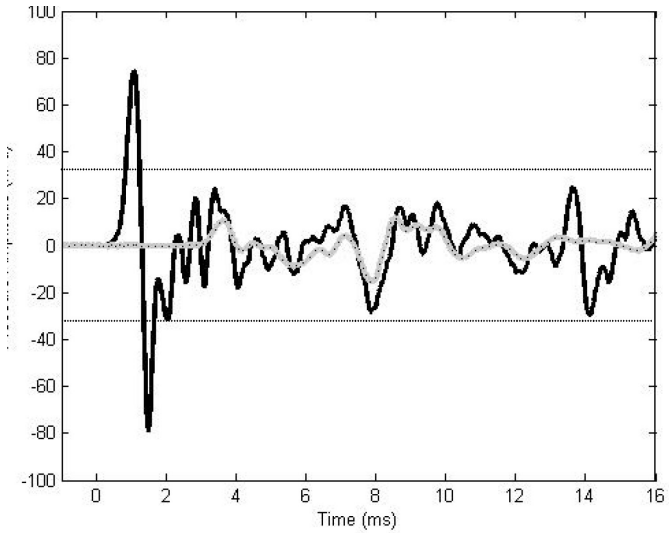

Figure 17. Acoustic pressure originating from an untreated pile (black line) and a pile surrounded by the TNAP (grey line) as recorded by a hydrophone in the VLA located 4.8 m off the bottom at a range of 12 m.

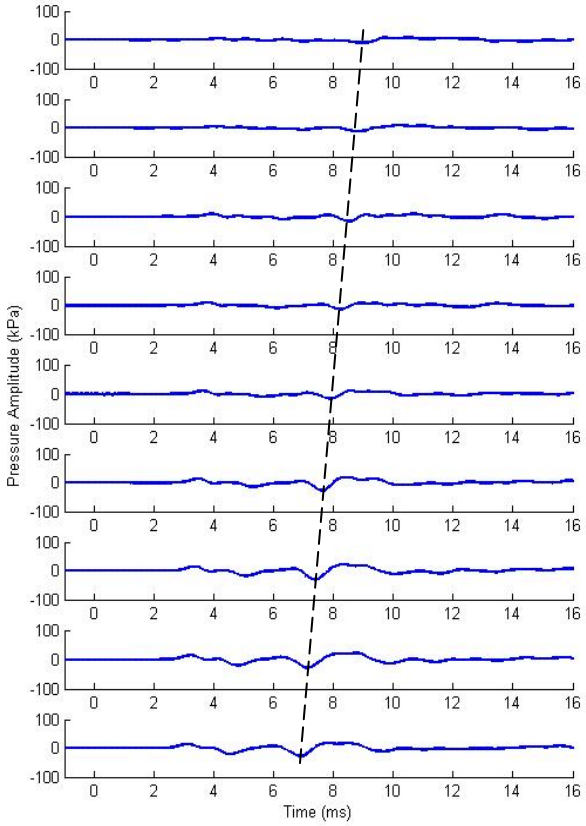

Figure 18. The acoustic pressure records from all nine hydrophones at a range of 12 m. The black dotted line connects the maximum amplitude peak recorded by all the hydrophones. It can be seen by the slope of this line that the Mach wave arrives at the lowest hydrophone first.

We conclude this section on the TNAP with s summary of all measurements made of untreated piles and TNAP piles at three ranges during the Vashon test (Fig. 19). Referring to the peak pressures, the differences between untreated and TNAP varies somewhat as a function of test range and depth of measurement, but it was consistently between 10 and 15 dB. On the other hand the differences for single strike Sound Exposure Level (SEL) were somewhat less, say 5 to 10 dB. This is understandable in view of the above discussion on how the TNAP system effectively blocked the first and peak arrival, but later arrivals that originate from the seabed and which all contribute to SEL, are not blocked.

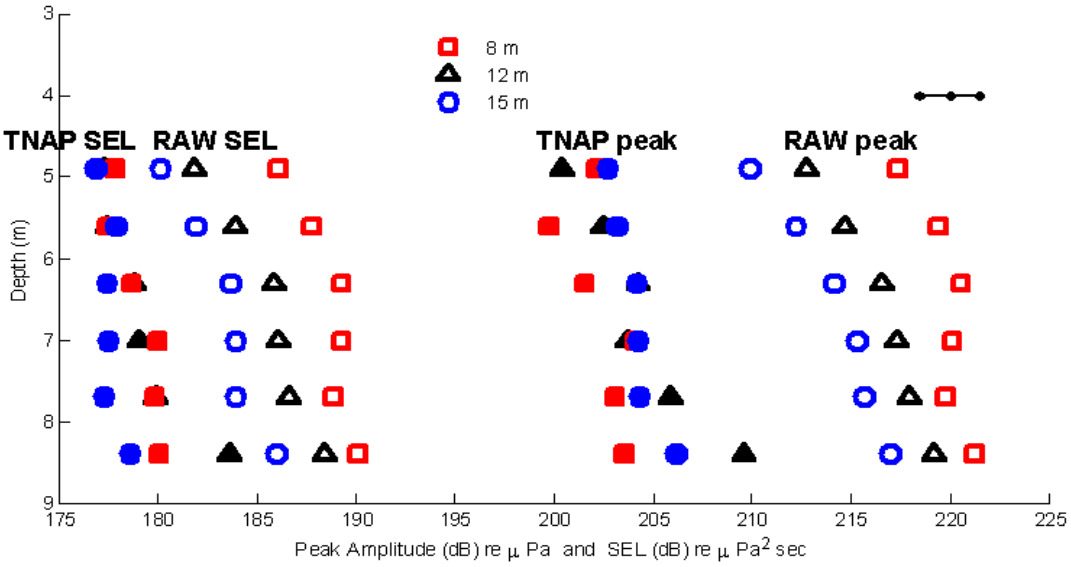

Figure 19. Summary of peak acoustic pressure and SEL for raw pile and TNAP cases measurements at Vashon at ranges 8, 12 and 15 m versus depth. Error bar in upper right corner applies to each data point.

4. TRANSMISSION LOSS FROM VIBRATORY PILING

In the following we present findings from an investigation of the transmission loss from a vibratory piling test off the Port Townsend Ferry dock conducted October 2010.

4.1. Data analysis

Figure 20 shows a histogram of short-time-averaged values expressed in dB of the signal centered at frequency 1000 Hz from vibratory pile driving measured at range 10 m. The key point here is that when processed to vary narrow bandwidths the range of variation is both quite large (~20 dB) but also very predictable. The theoretical prediction can be found in Dahl and Plant [11] which gives a standard deviation of 5.6 dB.

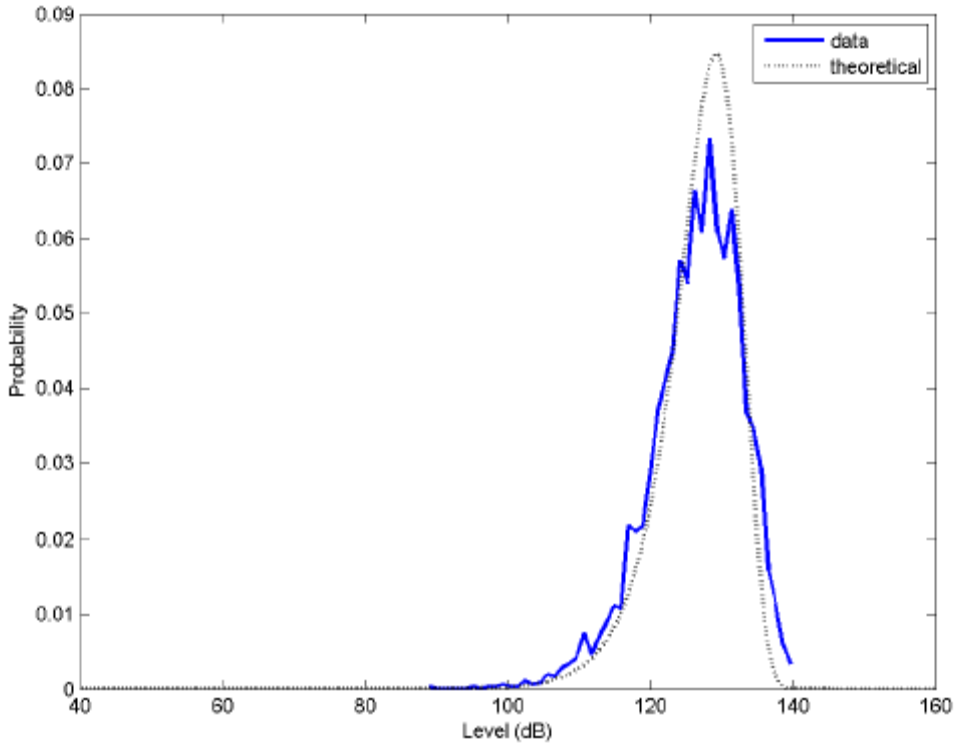

Figure 20 Narrow band received level in dB re 1 μPa, center frequency 1000 Hz, for vibratory pile driving measured at range 10 m.

Next, a similar histogram of short-time-averaged values is made from the same signal but at range 3200 m (Fig. 21). This data is governed by the same probability density function.

Transmission loss between 10 m and 3200 m is the decibel ratio of the two mean-square pressures involved, or equivalently, decibel subtraction of the data in Fig 20 from that shown in Fig 21. The resulting transmission loss histogram is shown in Fig. 22 and it has a theoretical standard deviation of $\sqrt{2}$ 5.56 dB.

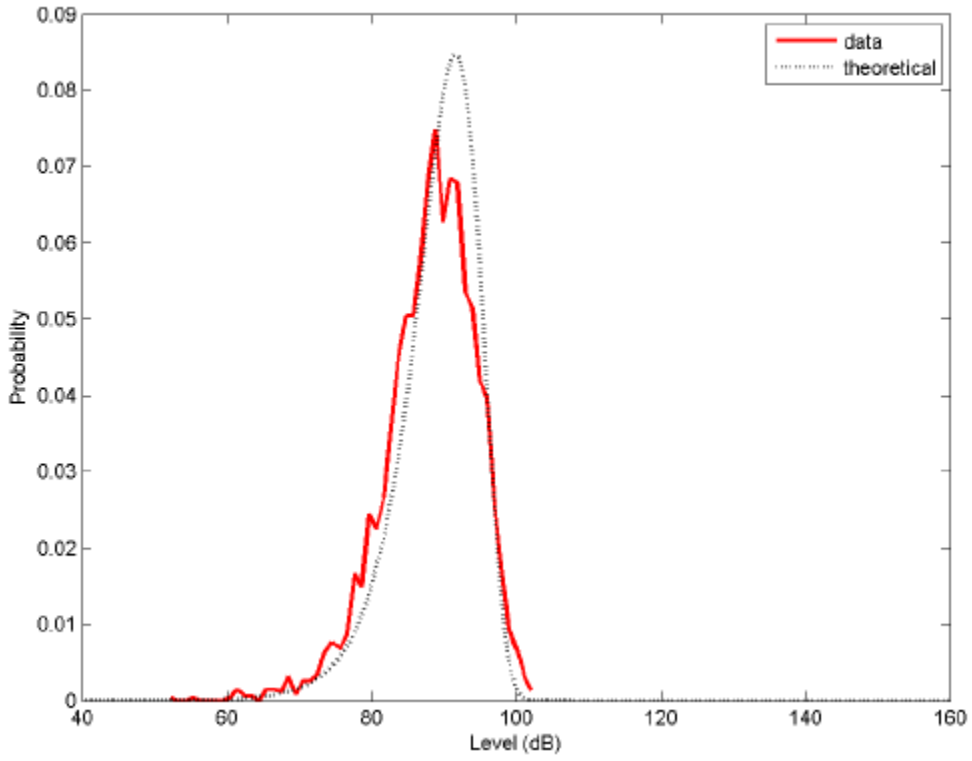

Figure 21. Narrow band received level in dB re 1 μPa, center frequency 1000 Hz, for vibratory pile driving measured at range 3200 m.

The key message from this study is that transmission loss is inherently quite variable, a fact should be appreciated when studies are made for which only a few observations are made. That said, the nature of this variation can both be understood and predicted, with

results going towards helping agencies make better use of monitoring resources. In the next section we address this briefly using state of the art acoustic modeling techniques.

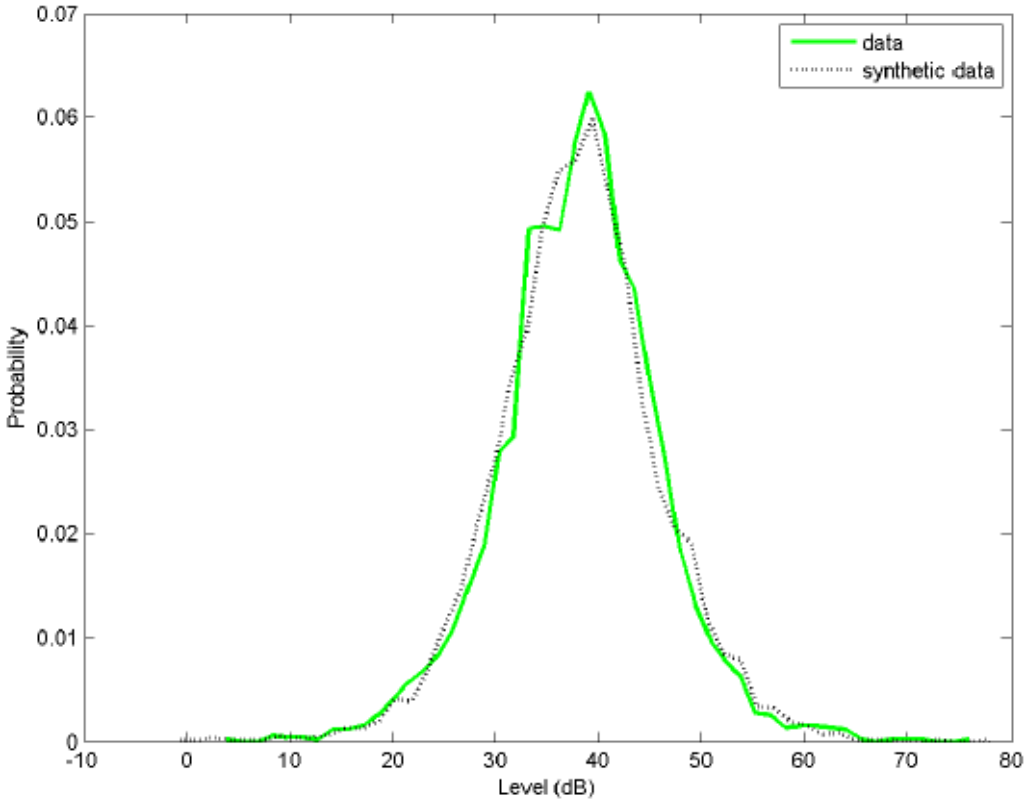

Figure 22. Histogram of narrow band transmission loss between range 10 m (Fig 19) and 3200 m (Fig 20), compared with theoretical value.

4.2. Studies using the Parabolic Wave Equation

The Port Townsend environment also showed considerable variation in bathymetry. This variation has impact in the prediction of mean transmission loss as is readily seen in Fig. 23. For example, depth-averaged transmission loss (red line, Fig 24) occasionally follows the so-called PSM, or Practical Spreading Model, (yellow line, Fig 24), but also frequently differs from the PSM by 10 dB or more. This is typically happens in areas associated with large changes in bathymetry. Other factors, such as sediment type (e.g., hard rock, sand, or muddy sediments) impact the over all transmission loss, and this

along with bathymetry needs to be included modeling. The result of better modeling will be more effective use of monitoring resources.

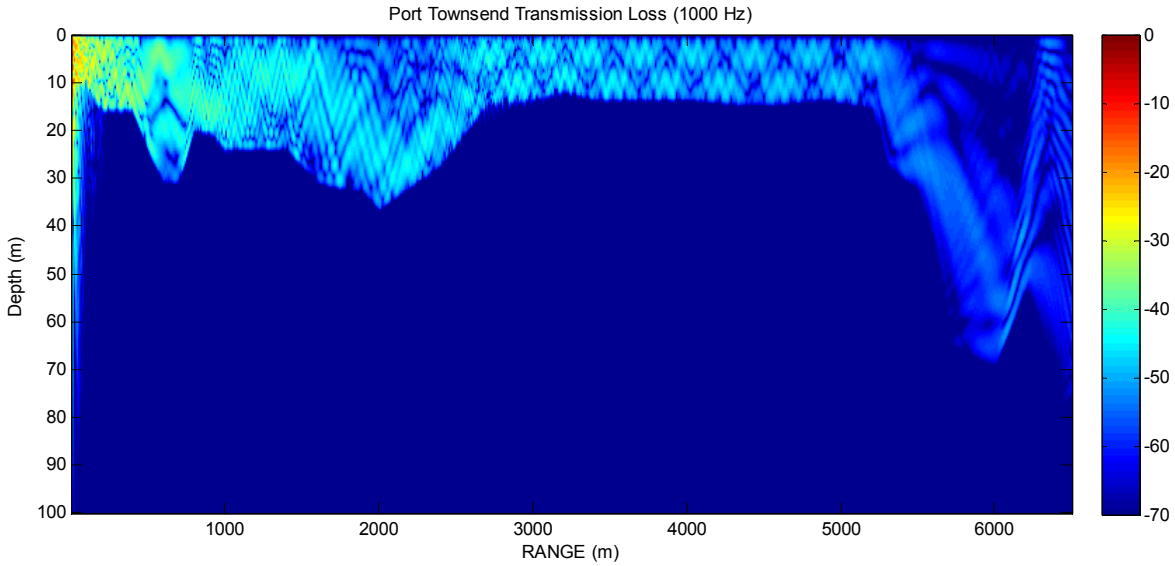

Figure 23. Transmission loss versus range and depth for the Port Townsend range based on available bathymetry and computed with the parabolic wave equation.

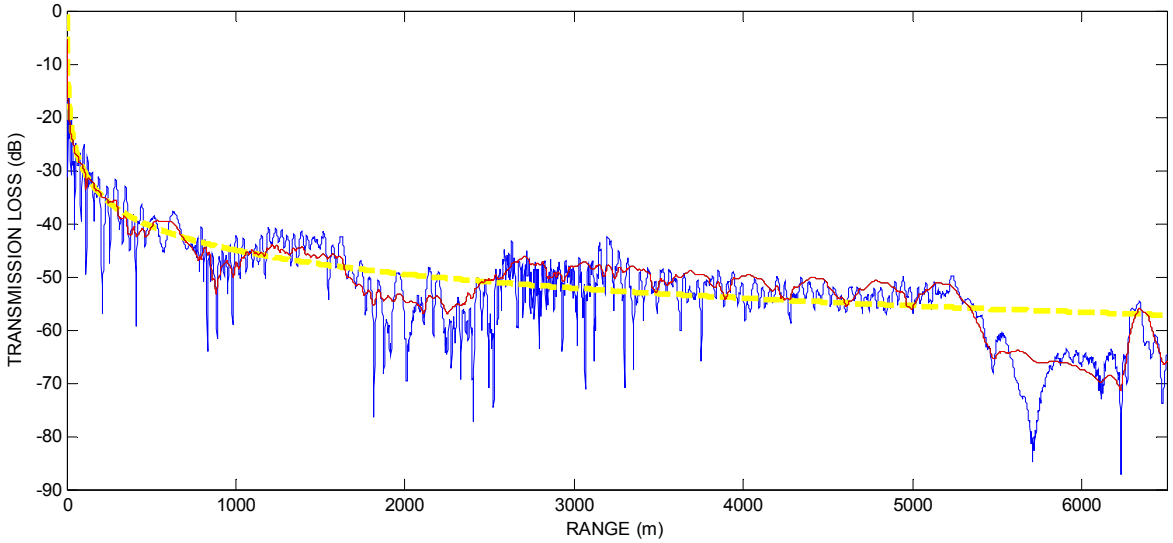

Figure 24. Transmission loss versus range at one depth 7 m (blue), depth average 0-10 m (red) and practical spreading model (yellow). The blue and red lines are derived from the results shown in Fig. 23.

Acknowledgments

This research was supported by the Washington State Department of Transportation with additional support from the Federal Highway Administration.

References

[1]C.A.F. de Jong and M.A. Ainslie, "Underwater radiated noise due to the piling of the Q7 Offshore Wind Park," In: Proceedings of the European Conference on Underwater Acoustic, Acoustics '08, M. Zakharia (ed), Paris, France, pp. 117-122, 2008.

[2]S. P. Robinson, P. A. Lepper, and J. Ablit , "The measurement of the underwater radiated noise from marine piling including characterization of the a 'soft start' period," In: Proceedings IEEE Oceans 2007, IEEE cat. 07EX1527C, ISBN: 1-4244-0635-8, 061215-074, Aberdeen, June 2007.

[3]P.T. Madsen, M. Wahlbert, J. Tougaard, K. Lucke and P. Tyack, "Wind turbine underwater noise and marine mammals: implications of current knowledge and data needs," Marine Ecology Progress Series, Vol. 309: 279-295, 2006.

[4]B.H. Fellenius,"Reflections on pile dynamics", Keynote paper to the 5th Int. Conf. on the Application of Stress-Wave Theory to Piles, Orlando, 1996.

[5]D.E. Weston, "Underwater explosions as acoustic sources," Proc. Phys. Soc. 76: 233, 1960.

[6]M. D. Collins, "A split-step Padé solution for the parabolic equation method," J. Acoust. Soc. Am. 93, 1736-1742, 1993.

[7] F.B. Jensen, W.A. Kuperman, M. B. Porter , and H. Schmidt, Computational Ocean Acoustics, American Institute of Physics, New York, 1994.

[8]K. L. Williams, D. R. Jackson, E. I. Thorsos, D. Tang, and S. G. Schock, "Comparison of sound speed and attenuation measured in a sandy sediment to predictions based on the Biot theory of porous media," IEEE J. Ocean. Eng. 27, 413-428, 2002.

[9]J. Zhou, X. Zhang, and D. P. Knobles, "Low-frequency geoacoustic model for the effective properties of sandy bottoms," J. Acoust. Soc. Am. 125, 2847-2866, 2009.

[10]J. Laughlin, Underwater sound levels associated with driving steel and concrete piles near the Mukilteo ferry terminal, WSF Mukilteo Test Pile Project, Final Report, March 2007

[11]P. H. Dahl and W. J. Plant, The variability of high-frequency acoustic backscatter from near the sea surface, ***J. Acoust. Soc. Am***., 101 (5), 2596-2602, May 1997.